

Thermo-mechanical analysis of road structures used in the on-line electric vehicle system

B.J. Yang^{1a}, S. Na^{2b}, J.G. Jang^{1c}, H.K. Kim^{3d} and H.K. Lee^{*1}

¹Department of Civil and Environmental Engineering, Korea Advanced Institute of Science and Technology (KAIST), 291 Daehak-ro, Yuseong-gu, Daejeon 305-701, Republic of Korea

²Korea Institute of Civil Engineering and Building Technology, 283 Goyangdae-ro, Ilsanseo-gu, Goyang-si, Gyeonggi-do 411-712, Republic of Korea

³School of Architecture, Chosun University, 309 Pilmun-daero, Dong-gu, Gwangju 501-759, Republic of Korea

(Received March 19, 2014, Revised November 9, 2014, Accepted November 11, 2014)

Abstract. On-line electric vehicle (OLEV) is a new eco-friendly transportation system that collects electricity from a power cable buried beneath the road surface, allowing the system to resolve various problems associated with batteries in electric vehicles. This paper presents a finite element (FE) based thermo-mechanical analysis of precast concrete structures that are utilized in the OLEV system. An experimental study is also conducted to identify materials used for a joint filler, and the observed experimental results are applied to the FE analysis. Traffic loading and boundary conditions are modeled in accordance with the related standards and environmental characteristics of a road system. A series of structural analyses concerning various test scenarios are conducted to investigate the sensitivity of design parameters and to evaluate the structural performance of the road system.

Keywords: on-line electronic vehicle (OLEV) system; precast concrete structure; thermo-mechanical analysis; experimental study; model sensitivity

1. Introduction

Environmental pollution associated with the use of fossil fuels has become a critical issue around the world, highlighting the necessity of green technology (Ahn *et al.* 2010). To overcome this issue, Korea Advanced Institute of Science and Technology (KAIST) introduced a novel on-line electric vehicle (OLEV) system, which relies solely on electricity, thus eliminating the need for fossil fuels. The OLEV utilizes the principle of inductive power transfer, where vehicles equipped with pick-up devices absorb electric power from cables underneath the road (Suh 2012). Since the batteries within the vehicle are recharged during operation on the road, the OLEV system

*Corresponding author, Professor, E-mail: leeh@kaist.ac.kr

^aPh.D. Candidate, E-mail: bumjoo@kaist.ac.kr

^bResearcher, E-mail: wongi@kict.re.kr

^cPh.D. Candidate, E-mail: jangjg @kaist.ac.kr

^dAssistant Professor, E-mail: hyeonki@chosun.ac.kr

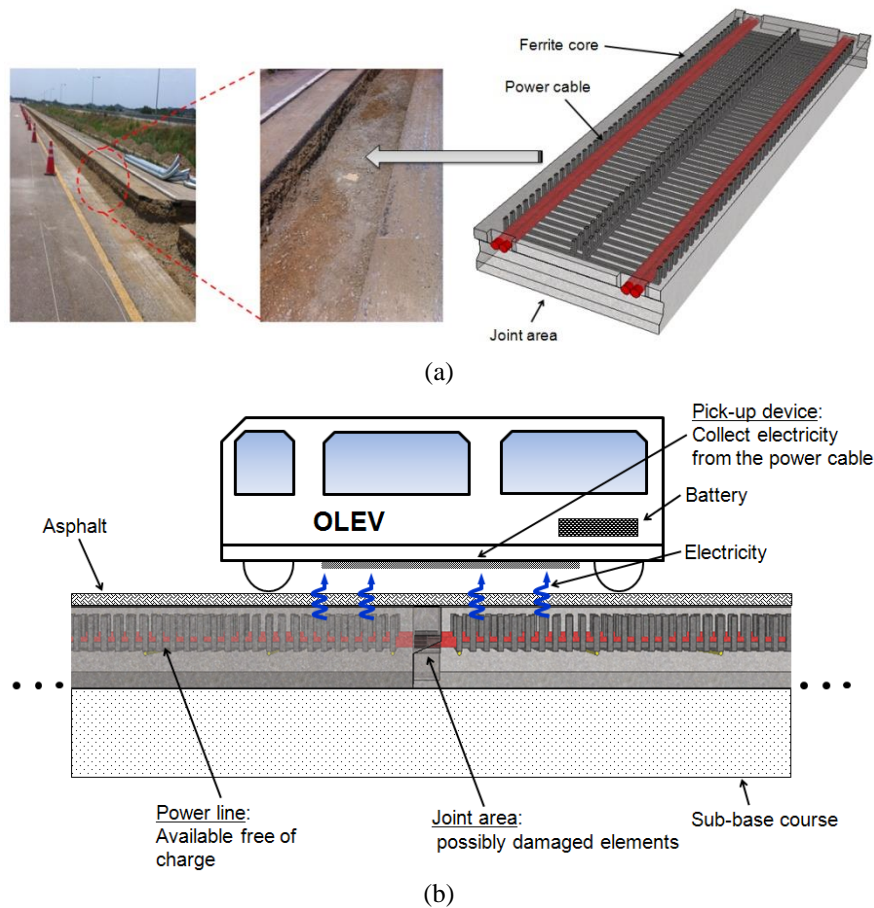


Fig. 1 Concept of the precast concrete structure for the OLEV system (cf., Cho 2012)

has advantages over conventional battery systems, including reduced battery weight, size, and recharging time (Cho 2012, Shin *et al.* 2012).

One of the key components of the OLEV system is the electrical power transferring system installed beneath the road. The road system is built from multiple precast concrete slabs for convenience at the construction site (Fig. 1). A continuous electrical power cable and a ferrite core that protects passengers from the magnetic field are installed in the road structure (Ahn *et al.* 2011), and the joint gap between precast concrete structures is filled with mortar material. Within the system, one of the factors that must be seriously considered is the damage between slab joints of the precast concrete structures due to the inhomogeneity of the road and continuous excessive loads from vehicles. It is thus important to create an optimal design for the road structure to protect the road system from failure, which can have devastating consequences.

The overall behavior of the OLEV system is also significantly affected by thermal stresses (Cho 2012). During the recharging process, wireless electrical power is transferred from the power cable to the OLEV, and the road system operates at a temperature of up to about 70°C (Tang *et al.* 2008, Ahn *et al.* 2011). The road structure is, thus, subjected to a large magnitude of heat flow; however, there is lack of information on the temperature distribution and thermo-structural

response of the OLEV system (Ellobody and Bailey 2011). The temperature-displacement relationship is predicted in the present study to provide useful insight into the behavior of the OLEV system under different thermal conditions.

Several theoretical and experimental studies have been carried out in recent years to evaluate the mechanical and thermal characteristics of road structures. Hu *et al.* (2013) proposed modeling strategies to analyze the stress concentration of the concrete road structure under traffic loading (Hu *et al.* 2013). Mo *et al.* (2007) suggested a model for a road system of porous asphalt concrete (PAC) that is able to predict the viscoelastic stress-strain responses of PAC under moving tire loads (Mo *et al.* 2007). They further conducted an experimental study to provide life predictions under complicated loading conditions, and investigated the effects of random stress and strain signals on mortar fatigue (Mo *et al.* 2013). In addition, finite element (FE) simulations considering various stiffness and thickness of the surface layer have been conducted to identify the load-carrying capability of the road structure (Wang *et al.* 2011). They concluded that the ideal modulus and thickness range of the surface layer was 2~2.5 GPa and 5~7 cm, respectively (Wang *et al.* 2011). More recently, Chen *et al.* (2013) studied the thermal effects on asphalt pavement in a temperature range of 25~50°C, and confirmed the significance of thermal effects on the road structure (Chen *et al.* 2013). Although various numerical and experimental studies on the road structures have been provided in literatures (Mo *et al.* 2007, Wang *et al.* 2011, Chen *et al.* 2013, Hu *et al.* 2013), ordinary structures without any electrical devices are mainly investigated. Since the present OLEV system is composed of the precast concrete structures and the electric recharging apparatus, additional numerical investigations considering the unique characteristic are carried out in the present study.

In this study, FE based thermo-mechanical analysis of precast concrete structures that are utilized in the OLEV system is presented. An experimental study is conducted to identify materials used for a joint filler, and the observed experimental results are applied to the FE analysis. The nonlinear material characteristics of concrete are modeled based on a smeared crack model (Boumiz *et al.* 1995, Lee 2009), and the model parameters are inversely estimated from experimental data. The boundary conditions and loading characteristics are also described in accordance with the system environment. Based on the proposed approaches, various test scenarios are simulated to search for factors that can increase the structural performance of the road system. In particular, the mechanical stresses induced by traffic loads are predicted via FE analysis. Furthermore, the distributions of heat flow and the thermal stresses of the OLEV system considering different travelling heat cases are predicted in the present study.

2. Test methodology and results

An experimental study was carried out as illustrated in Fig. 2. In the test, the specimen was assembled with two precast concrete slabs and a mortar joint, where each slab and the mortar joint have a hole in the middle region (Kim *et al.* 2012). A fiber-reinforced polymer (FRP) pipe with an inner diameter of 3.2 cm was then inserted through both concrete slabs and the mortar joint. The precast concrete slabs, made from ordinary Portland cement, were manufactured using a specially designed mold (Fig. 2(a)). The mix proportion and measured compressive strength of the precast concrete are listed in Table 1.

It is clear that the most vulnerable part of the OLEV road system is the joint area which connects the precast concrete slabs. The selection of the mortar material is therefore important for

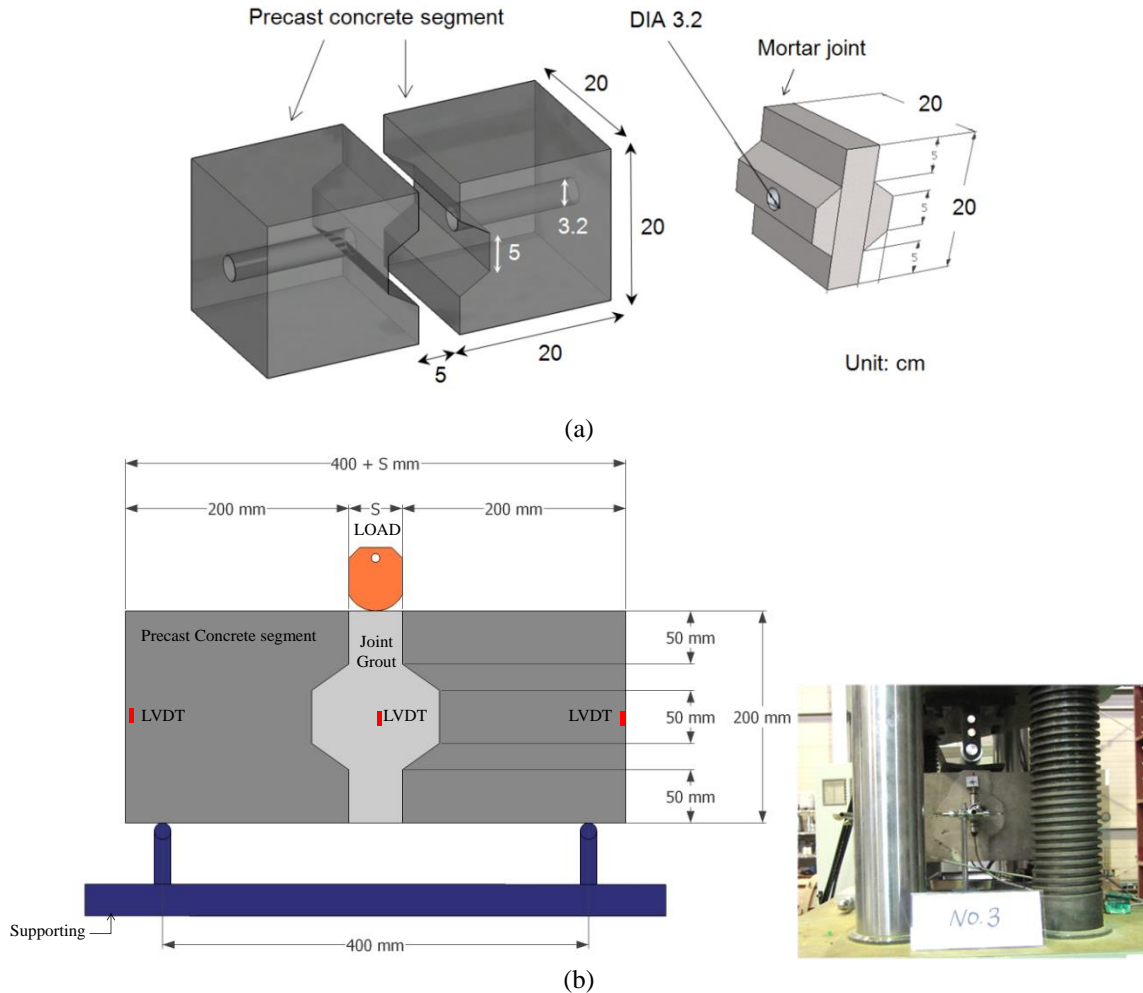


Fig. 2 (a) Geometry of the specimen used in experiment and (b) experimental setup of three-point bending test

Table 1 Mix proportion and measured compressive strength of precast concrete

W/C	S/a	Unit weight (kg/m ³)					Compressive strength (MPa)**	Flexural strength (MPa)**
		Water	Cement	Sand	Gravel*	Super-plasticizer		
35	38.3	171	488	620	1015	3.22	40	5.4

*G_{max}=25 mm, ** Measured at age of 28 day

the overall stability of road structures, and the following conditions should be fulfilled: (a) a small ratio of shrinkage in the mortar, (b) a similar stiffness to that of the precast concrete to prevent stress concentration, and (c) a high level of mortar fluidity for enhanced workability.

Accounting for the aforementioned criteria, three different mortar materials were considered in the experimental study: ordinary cement mortar (OCM), non-shrinkage cement mortar (NCM),

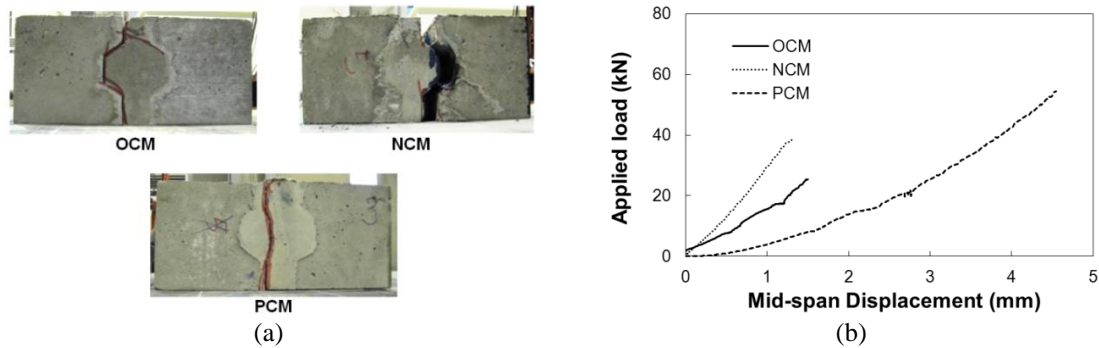


Fig. 3 (a) The failure modes of the specimens assembled with two precast concrete slabs and different mortar joints and (b) the force-displacement relationship of specimens under three point flexural tests

Table 2 Mix proportion and measured compressive strength of precast concrete

Specimen code	Peak load (kN)	Displacement at failure (mm)	Flexural Strength (MPa)	Failure mode
OCM-S	25.38	1.42	1.90	Bond
NCM-S	38.71	1.35	2.90	Bond
PCM-S	54.49	4.54	4.09	Flexural

and polymer cement mortar (PCM). The flexural behavior of the specimens was evaluated by a three- point bending test, as shown in Fig. 2(b). Here, the specimen was loaded on the frame of a 200 kN universal test machine (UTM), and three linear variable differential transformer (LVDT) were attached, one on the center of the joint area, and two equally spaced from the center piece on each concrete slab. Note that three sets of each specimen type are fabricated, and total of nine specimens are prepared for testing the load-displacement behaviors. The averaged value from the experimental measurements is given in Fig. 3 and Table 2.

The failure modes of the specimens are shown in Fig. 3(a). It can be seen from the figure that the OCM and the NCM specimens (OCM-S and NCM-S) are ruptured by debonding failure between the concrete and the mortar, thus indicating that the adhesion strength at the joint region is lower than the flexural strength of the overall structure. In contrast, the PCM specimen (PCM-S) exhibits flexural failure behavior; a crack in the PCM initiated from the bottom of the segment, and linearly grew along the external top-surface. The force-displacement relationship of the specimens under a three point flexural test is shown in Fig. 3(b).

From the results of the flexural test, the segment with PCM is chosen as the joint filler for the structure for the following reasons:

- (i) The maximum strength of the PCM-S was much higher (54.49 kN) than that of the OCM-S and NCM-S (23.58 and 38.71 kN).
- (ii) In terms of maximum deflection, the specimen filled with PCM exhibited better performance (4.54 mm) compared to specimens with OCM and NCM (1.42 and 1.35 mm).
- (iii) The inhomogeneous segments with OCM and NCM do not behave as a monolithic structure; however, the PCM-S retains sufficient adhesion strength to behave as a monolithic segment, resulting in higher strength of the overall structure.

The test results including peak load, failure displacement, flexural strength, and failure mode are summarized in Table 2.

3. Modeling descriptions

In the present FE simulation, the smeared crack model of concrete (Bazant and Oh 1983, Boumiz *et al.* 1995) is adopted to consider the nonlinear behavior of the concrete, and the model parameters are inversely estimated from experimental data. A three-dimensional finite-element (FE) mesh is built using the commercial code ABAQUS (ABAQUS 2005), and the linear-elastic material properties including the Young modulus E_c and the Poisson's ratio ν_c of concrete used in the current model read: $E_c=28$ GPa and $\nu_c=0.18$. In addition, the Young's modulus and the Poisson's ratio of the ferrite core are adopted from Lee (2009) as $E_f=150$ GPa and $\nu_f=0.30$, while those of PCM mortar are $E_m=22$ GPa and $\nu_m=0.18$ (Islam and Khennane 2013).

The contact surface between the concrete slabs and the mortar is particularly modeled by the interaction options in the FE code ABAQUS (ABAQUS 2010). The hard contact option is utilized for the normal direction response, while the penalty option is adopted along the direction tangential to the interface with a friction coefficient of 0.65 (Zhou and Young 2012, Tahmasebinia *et al.* 2013). The hard contact modeling in the commercial FE software ABAQUS is provided as (ABAQUS 2010)

$$\delta\Pi = \delta p \cdot h + p \cdot \delta h$$

with

$$\begin{cases} p = 0 \text{ for } h < 0, & \text{contact is open} \\ h = 0 \text{ for } p = 0, & \text{contact is closed} \end{cases}$$

where Π denotes the contact virtual work contribution, p is the contact pressure, and h is the overclosure (ABAQUS 2010). The opposite end lines of the mesh were constrained vertically, restricting the movement of the model during the simulation period ($u_z=0$; Huang *et al.* 2007). More detailed theoretical derivation of the formula can be found in ABAQUS Theory Manual (ABAQUS 2010).

The opposite end lines of the mesh were constrained vertically, restricting the movement of the model during the simulation period (Huang 2007, Yang *et al.* 2014). The force versus displacement relationship obtained from the measurement and the numerical prediction are depicted in Fig. 4(a). The constants of the smeared crack model are specified through comparison between experimental study and the numerical prediction, and the fitted values are applied to the present study. The measured and fitted curves are not in close as shown in Fig. 4(a), whereas the fracture strengths and displacements of PCM-S match quite well. Although the present study intends to estimate the most vulnerable location of the OLEV system, further efforts are needed for more accurate analysis of the OLEV system. Fig. 4(b) shows the von-Mises effective stresses in the deformed shape, where blue and red colors denote low and high stresses, respectively. Note that the mesh size in the simulation is equal to 0.08 m that is determined by a mesh sensitivity test. The detailed process and result of the parametric study are addressed in Section 4.

When the road structures are buried underground, both the slabs and surrounding soil are influenced by the external loads (Jayalekshmi *et al.* 2013, Zhu *et al.* 2014). In order to model the binding characteristic of soils, the boundary condition is assumed as a support condition, which implies the modulus of resilient and subgrade reaction at the ends of the member. The resilient modulus that represents the restitution force of the soil layer is applied on the surface on the x -axis (Fernlund *et al.* 2003, Kwasniewski *et al.* 2006), and the constants of the resilient modulus, mechanical properties, and thickness of each soil layer are listed in Table 3 (Lee 2012). In

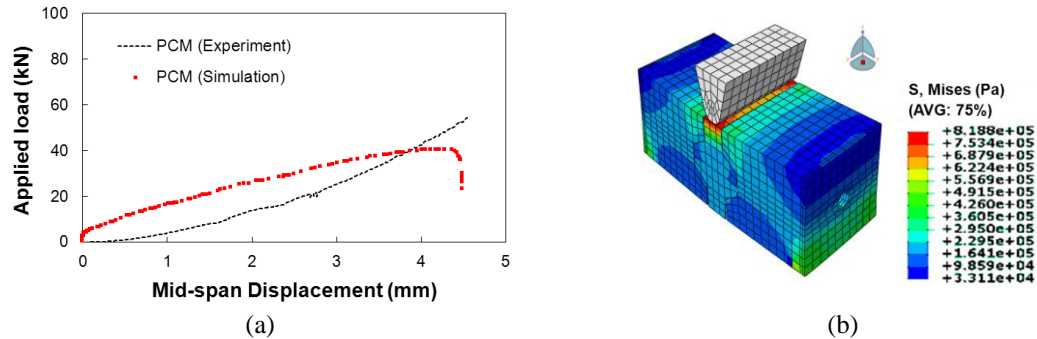


Fig. 4 (a) A comparison of the force-displacement relationship between the experimental and numerical results and (b) a von-Mises effective stresses in the deformed shape of specimen filled with PCM-S

Table 3 Material properties and resilient moduli of the road layer (Lee 2012)

	Young's modulus (MPa)	Poisson's ratio	Thickness (mm)	Resilient modulus (MPa)	
				Summer	Winter
Surface layer	4000	0.30	100	0.985	11.252
Base course	4000	0.30	200	1.125	7.032
Sub-base course	400	0.35	300	0.141	0.141
Subgrade	15	0.40	9650	31.600	31.600

Table 4 Standards of the traffic loading applied in the present study (Lee 2009)

	Total weight of truck (ton)	Weight (ton)			Width (mm)		Tread (mm)
		Front wheel (0.1W)	Middle wheel (0.4W)	Rear wheel (0.4W)	Front wheel (0.1W)	Rear wheel (0.4W)	
DB-24	43.2	2.40	9.6	9.6	125	500	200
DB-18	32.4	1.80	7.2	7.2	125	500	200
DB-13.5	24.3	1.35	5.4	5.4	125	500	200

particular, the resilient moduli measured in summer are applied in the simulation accounting for the weakest condition of the soil. Similarly, the modulus of the subgrade reaction is applied at the bottom of the sub-base course as $k=6.818 \text{ kg/cm}^3$ (Lee 2012, Islam and Khennane 2013). Throughout the analysis, the external load is modeled as the pressure, which is defined as $P=0.9408 \text{ MPa}$ over an area of $20 \times 50 \text{ cm}^2$ (Lee 2009) considering a vehicle weight of 43.2 tons for a truck (Table 4).

Furthermore, in the present study, two different designs for the slab joints are investigated, Design I (D_1) and Design II (D_2), where D_2 model is further divided into three sub-models ($D_{2-1,2,3}$), as illustrated in Fig. 5. The D_1 model is known to have the advantage of easy integration with other power cables in nearby segments, whereas the manufacturing work is quite cumbersome. On the other hand, the D_2 model has much more convenient design features compared to the D_1 ; however, one issue with the D_2 model is the possibility of a local damage at the slab joints due to its shape (Cho 2012). Both the D_1 and D_2 models are analyzed via FE-based simulations. With the results, the proper and optimized design of the road structure is proposed, which is crucial for the application of the OLEV system. The number of element used in the

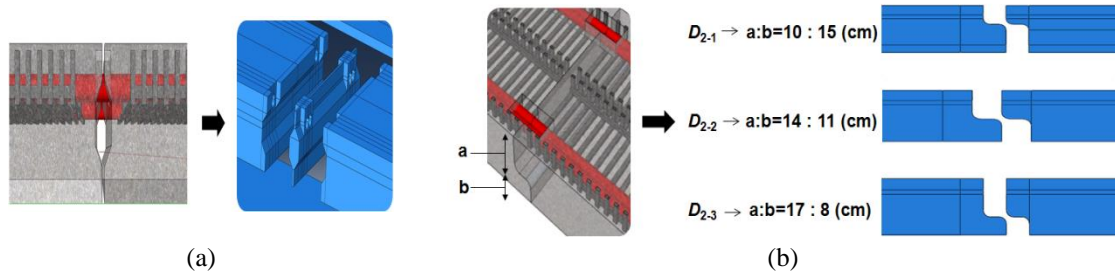


Fig. 5 (a) Schematics of the road structure of D_1 and (b) $D_{2-1,2,3}$ models

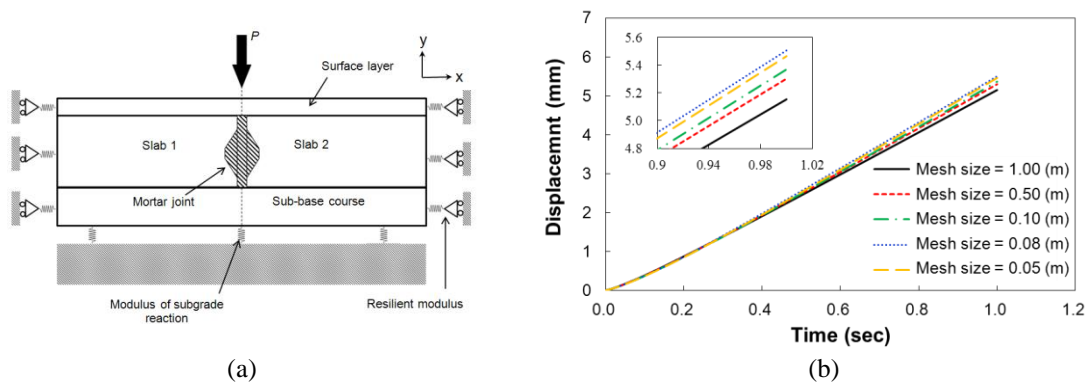


Fig. 6 (a) A schematic layout of the simulation and (b) predicted displacements with different levels of mesh refinement

present simulations is dependent on the design of mortal types, and is approximately 35000~40000. The FE mesh size throughout the analysis is fixed to be 0.08 m based on the mesh sensitivity test given in Fig. 6.

4. FE analysis of structural performance

4.1 Design sensitivity

First, a mesh sensitivity test is carried out for a preliminary study. The road structure is set to be two connected slabs with the ferrite core, mortar, surface layer, and sub-base course (Fig. 6(a)). The static loading of P is then applied on the road system. The D_1 model with various levels of mesh refinement is utilized to determine the optimal density of the mesh scale, and the predicted displacements are illustrated in Fig. 6(b), showing that the displacements converge when the mesh size is 0.05 m. Considering the computational efficiency, the FE mesh size is fixed to be 0.08 m throughout the analysis (Liang *et al.* 2006, Lee *et al.* 2007). Here, the averaged displacements occurred at points 1 and 2 are considered in the test, and the specific locations of the points are illustrated in Fig. 7.

For investigation of how the joint design affects the overall behavior of the recharging road structure, different designs of the concrete slab (D_1 and $D_{2-1,2,3}$) subjected to the traffic load, P , are

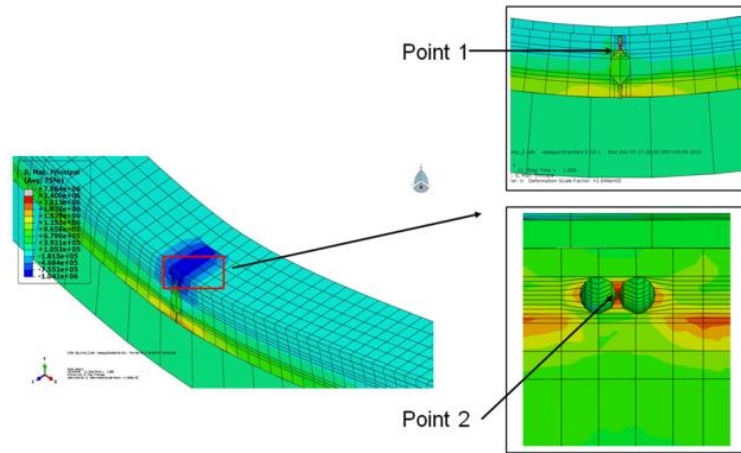


Fig. 7 The representative distribution of the maximum principal stress on the FE model and points of comparison

Table 5 FE analysis results under a static load

	Displacement (mm)	Max. principal stress at Point 1 (MPa)	Max. principal stress at Point 2 (MPa)
D_1	5.420	2.292	2.512
D_{2-1}	4.921	1.824	2.138
D_{2-2}	4.918	1.209	3.156
D_{2-3}	4.905	1.032	3.672

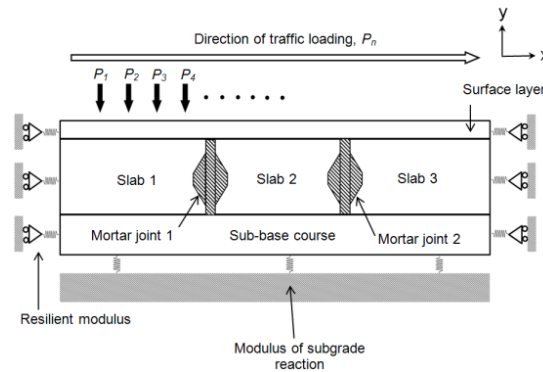


Fig. 8 Schematic configuration of the model subjected to dynamic traffic load

simulated. The aforementioned boundary conditions are adopted here, and the static loading ($P=0.9408$ MPa over an area of 20×50 cm²) is applied to center of top surface of the structure. It is shown from Fig. 7 that stresses are mainly concentrated near the joint area (point 1) and the cable hole (point 2), and results at these points are listed in Table 5. It is noted from Table 5 that the stress occurring near the cable hole is much higher than those at the joint area. Also, for the $D_{2-1,2,3}$ models, it is observed that the stress at the joint area decreases as the depth ratio of the joint (a/b) continues to increase, whereas the stress near the cable hole increases when the effective depth

ratio (a/b) increases.

Moreover, numerical tests subjected to the sequential traffic load are carried out. This simulation is based on a wheel load tester, which is a machine that is used for testing and evaluating mechanical failures of road structures (Bechtoula *et al.* 2009, Song *et al.* 2005). Three-connected concrete structures are considered in the test, and the schematic configuration of the simulation is depicted in Fig. 8. Identical boundary conditions, loads, and mesh scales are applied in the simulation. The sequences of the deformed shape and maximum principal stress of the D_1 model are displayed in Fig. 9, and the simulation results of D_1 model are shown in Fig. 10(a). It can be observed that the maximum value of the stress arises near the power cable area, and the predicted values exceed the results from the static load simulation. The time-displacement relationship at point 1 is presented in Fig. 10(b).

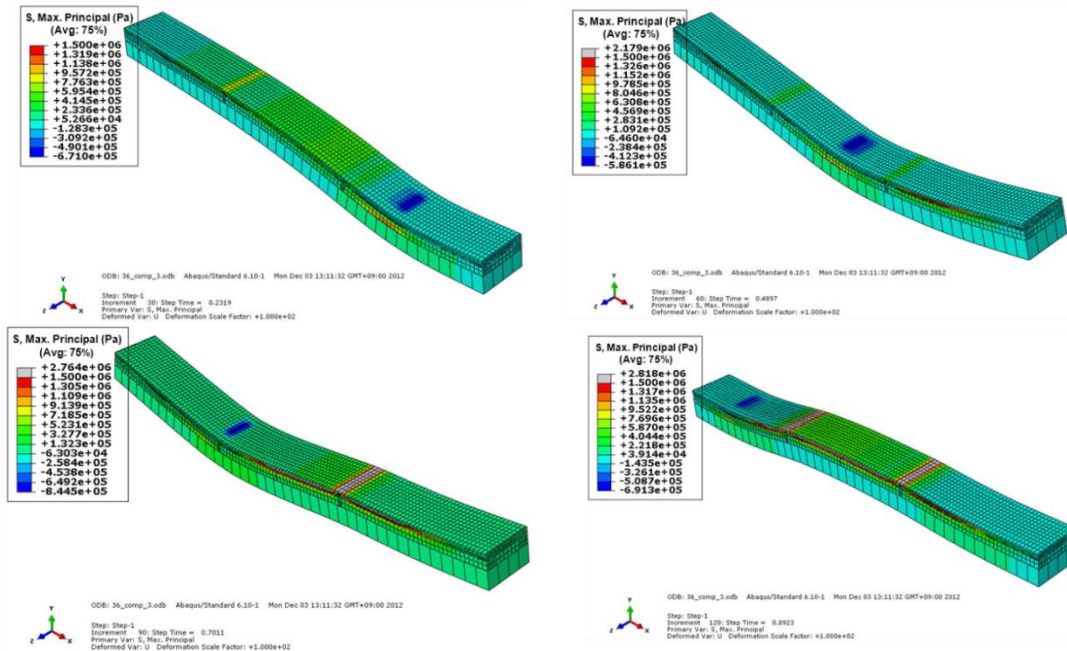


Fig. 9 The representative deformed shape and maximum principal stress under traffic loading

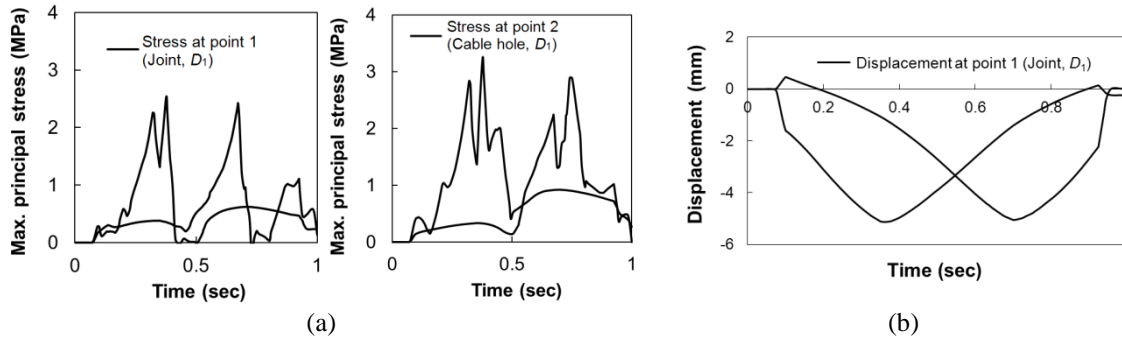


Fig. 10 (a) Time-maximum principal stress relationship at point 1 (joint) and point 2 (cable hole), and (b) time-displacement relationship at point 1 for the D_1 model

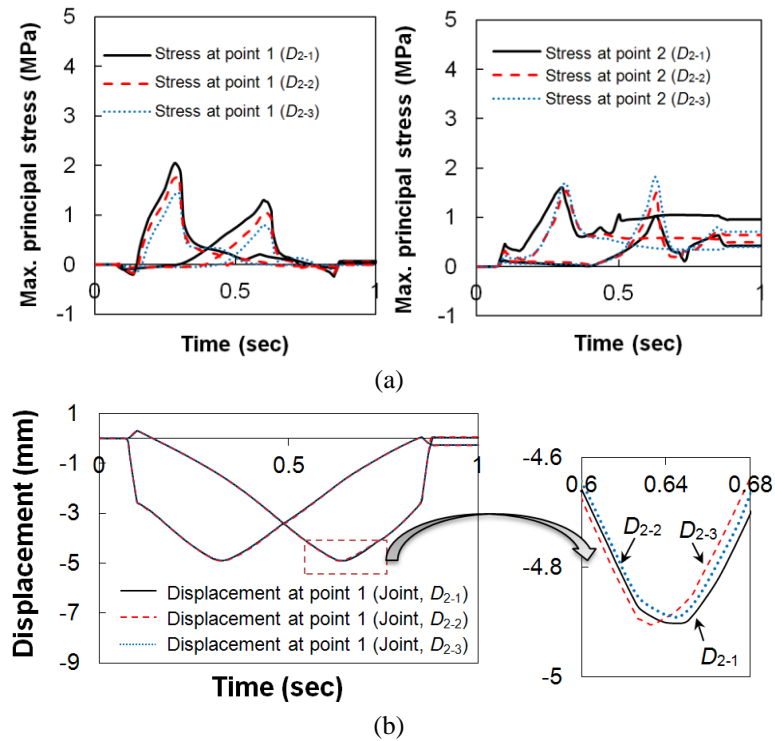


Fig. 11 (a) Time-maximum principal stress relationships at point 1 and point 2, and (b) time-displacement relationships at point 1 for the $D_{2-1,2,3}$ models

In case of the models of $D_{2-1,2,3}$, the time-stress relationships induced by traffic loading are plotted in Fig. 11(a). These figures indicate that the tendencies of the analysis results are similar to those obtained in the static load simulation. The stress near the power cable tends to increase with an increase in the depth ratio (a/b) of the joint; however, the stress at the slab joints decreases as the depth ratio (a/b) increases. In addition, the time- displacement relationships at the joint area for the $D_{2-1,2,3}$ models are plotted in Fig. 11(b), showing slight differences in the models. Based on the numerical simulations, it is noted that the mechanical behavior of the road structures is somewhat affected by the shape of the slab joints and that this influence is more influential in the area near the power cable.

4.2 Various test scenarios

Additional numerical simulation of the road structure under various loading schemes is simulated to estimate the structural perturbations in a realistic environment. The layout of the simulation, as shown in Fig. 12, consists of a single lane road section embedded in three connected concrete slabs. The loading types are classified as Case 4 according to the loading location of the vehicle. Case 1 represents the general case of loading condition on the road, while the traffic loading is applied to the edge of the road that is nearby the segments in Case 2. Case 3 illustrates that the loading is applied to the intermediate location between the segment and the road. Lastly, it is shown in Case 4 that the traffic loading is applied to the center of the road structure, which is

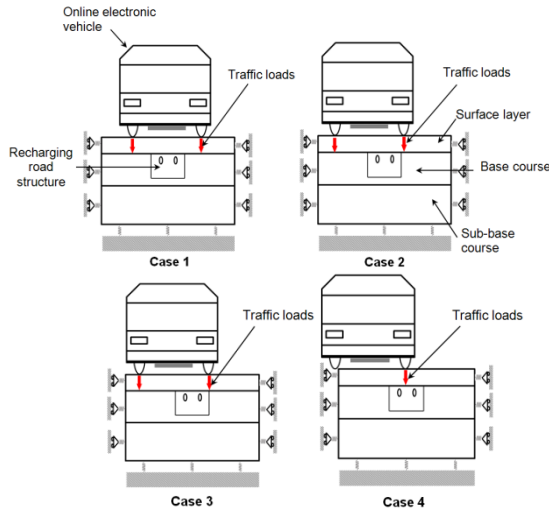


Fig. 12 Layout of modeling compositions with various loading locations

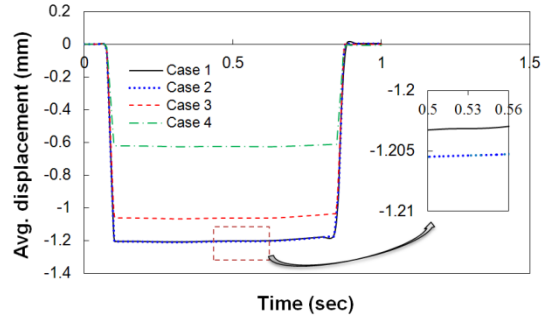


Fig. 13 Predicted average displacement-time relationships at the stair gap

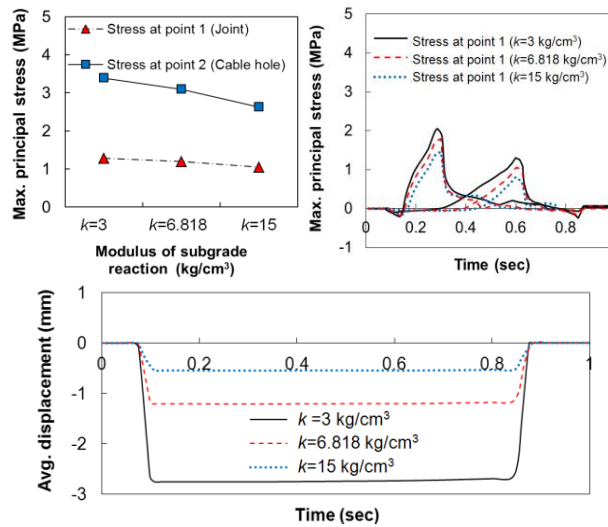


Fig. 14 The results of FE simulations of the road structure with various subgrade reaction factors

directly above the precast segment.

The $D_{2.2}$ model, which exhibits the average performance among all models, is selected in this simulation. The numerical results, showing the average displacement at the stair gap, are plotted in Fig. 13. From the simulation, it is noted that the smallest displacement is observed when the Case 4 loading condition is imposed on the roads, whereas the largest displacement is predicted for Case 4. Furthermore, the response for Case 4 lies between those pertaining to the curves, and the prediction for Case 4 is analogous to that of Case 2.

Considering the application of the structural analysis, it is desirable that these assessments are done under different environmental conditions to improve the value of the present study. As

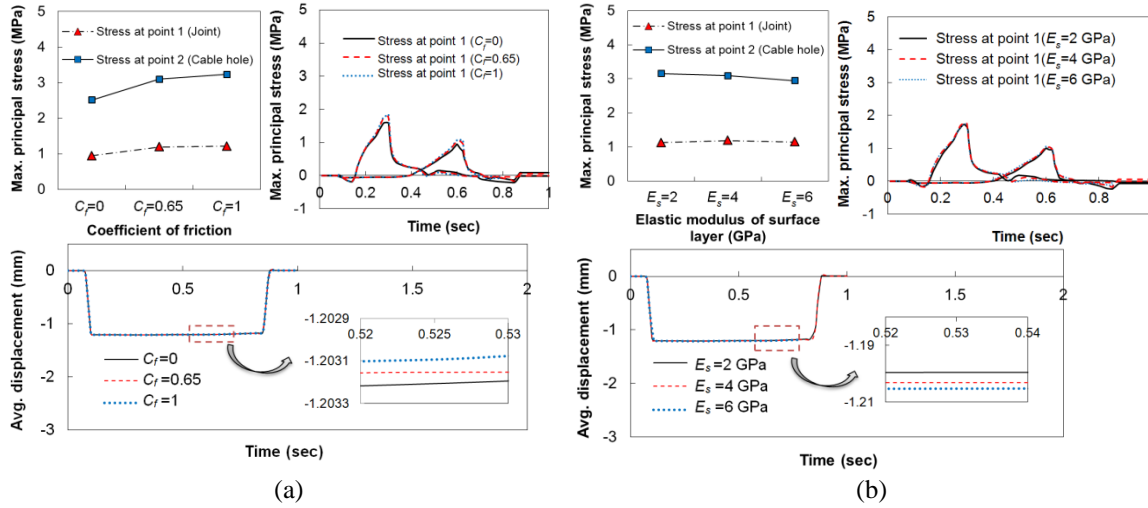


Fig. 15 The FE predicted results of the road structure (a) with variation of the friction coefficient between the slab joints and (b) with varying elastic modulus of surface layer

mentioned earlier, the modulus of subgrade reaction (k) is applied at the bottom of the sub-base course to describe the subgrade. The magnitude of the subgrade reaction modulus signifies the compaction condition of the soil; a higher value of the modulus denotes a high degree of compaction. In order to estimate the optimal compaction degree, numerical tests while varying the subgrade reaction modulus are performed, as shown in Fig. 14. The results show that the modulus of the subgrade reaction is clearly related to the mechanical performance of the recharging road structures, especially being quite influential on the stair gap between the segments and the soil layers.

Figs. 15 and 16 show the simulation results of the road structure with different levels of the friction coefficient (C_f) and the stiffness of the surface layer (E_s), respectively. Fig. 15 shows the tendencies of the numerical results, showing that the friction coefficient at the contact area does not influence the structural responses. Fig. 16 also shows various mechanical behaviors with respect to elastic modulus of the surface layer. It is observed from Fig. 16 that the effect of the surface layer is insignificant on the overall behavior of the road system, similar to the effect of the friction coefficient. These results indicate that the enhancement of bonding properties at the contact area and the stiffness of the surface layer may be less important but that improving the compaction level of the subgrade soil is vital.

5. Thermal analysis

The electrical power cable embedded in the precast road structure generates a high degree of heat dissipation when the recharging operation is performed (Cho 2012), and it is believed to lead a significant reduction in strength and stiffness of OLEV system (George and Tian 2012). To assess the thermal effects on the OLEV system, numerical analysis of the road structure is carried out in the current study. The heat flow of the two-connected D_{2-2} model is tested according to the external temperature when the model is assumed to be buried underground (Ronagh and Behnam

Table 6 Temperature data adopted in the simulations (Shin *et al.* 2011)

	Temperature (°C)	
	Summer	Winter
Atmosphere	32.0	-12.5
Surface layer	46.0	-10.0
Base course	42.5	-7.0
Sub-base course	31.0	-4.0
Subgrade	30.0	-2.5

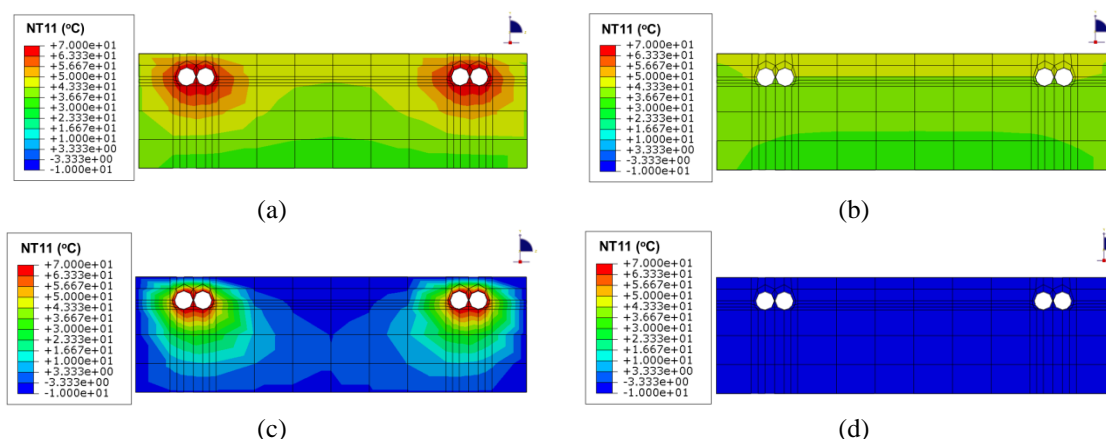


Fig. 16 The distributions of heat flow in the segment with respect to thermal conditions: (a) prediction with considering heat generation at summer, (b) prediction without considering heat generation at summer, (c) prediction with considering heat generation at winter, (d) prediction without considering heat generation at winter

2012). In order to take into account the worst-case scenario, only the recorded data at the lowest winter temperature and the highest summer temperature are considered here. The experimentally measured temperature data for each soil layer is applied to the surface of the road structure, and the temperature data are listed in Table 6 (Shin *et al.* 2011). The analysis is separately carried out in the case of power cable temperature at 70 °C and at ambient level. Hence, the thermal analysis is performed for the case of four (Fig. 16). The same boundary conditions with the structural analysis are applied in the thermal analysis, and the detailed descriptions of the boundary conditions are explained in Section 3.

The thermal conductivity of the concrete material is taken from literature (Kim *et al.* 2003) and is given as 1.4 W/m°C. Fig. 17 shows the distributions of heat flow in the segment with varying thermal conditions. It is found that the concentrated heat at summer is generally less than that at winter, while the effects of power cable heat is much influential at summer (Zou *et al.* 2013). Based on the calculated heat distribution, the thermal expansion in the OLEV system is simulated. The coefficient of thermal expansion of the concrete is set to be $1.1 \cdot 10^{-5} / ^\circ\text{C}$ on reference to Sellevold and Bjontegaard (2006). In addition, the following parameters are adopted for the thermo-mechanical analysis: $g=9.8 \text{ m/s}^2$, $\rho_c=2300 \text{ kg/m}^3$, $E_c=28 \text{ GPa}$ and $\nu_c=0.18$, where g denotes the gravity force; ρ_c , E_c and ν_c are the density, elastic modulus and Poisson's ratio of the concrete material, respectively. Table 7 and Fig. 17 show the predicted strain distributions induced by

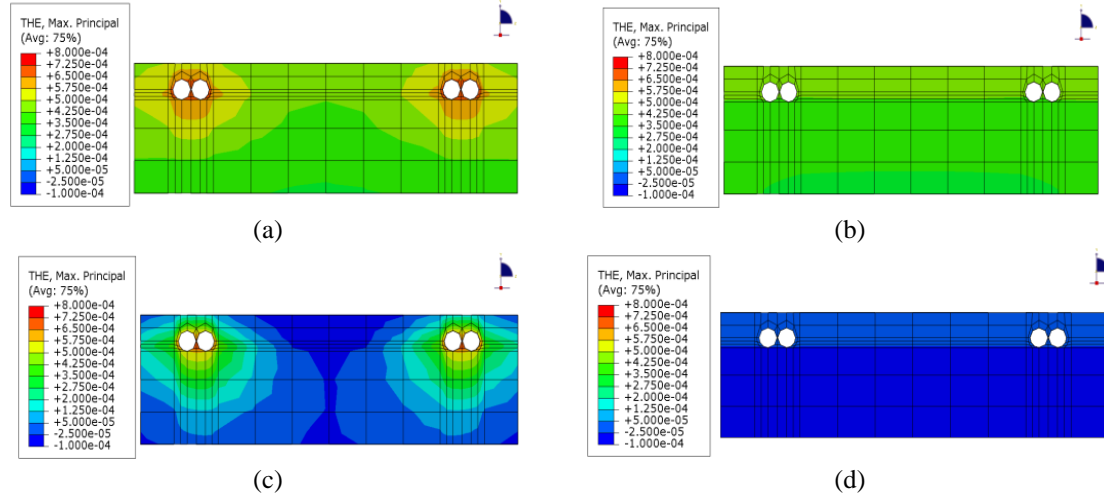


Fig. 17 The predicted thermal strain in the segment with varying environmental conditions: (a) prediction with considering heat generation at summer, (b) prediction without considering heat generation at summer, (c) prediction with considering heat generation at winter, (d) prediction without considering heat generation at winter

Table 7 Predicted displacements with various thermal conditions

	Displacements (mm)
Case 1 (Summer, cable heating)	3.667
Case 2 (Summer)	1.646
Case 3 (Winter, cable heating)	1.378
Case 4 (Winter)	0.644

thermal stresses. It is observed that the thermal strain is occurred as a whole over the structure, and the displacement levels are relatively less compared to that of mechanical loading. Furthermore, it is found that the maximum displacements increase nearly twice when heat dissipation from the power cable occurs.

6. Conclusions

In this study, a FE based thermo-mechanical analysis is conducted to assess the overall behavior of the recharging road structures for a new eco-friendly transportation system (OLEV). In order to determine the nonlinear material properties of concrete, an inverse analysis is performed and the results are compared with those of an experimental study. Several three-dimensional FE meshes of the road structure are generated and a series of numerical simulations with different conditions are carried out to identify factors that can increase the stability of the road system. This study extends over the mechanical analysis and predicts the thermal distribution throughout the road structures at different cases of heat travelling between the electrical power cable and the external surface of the structure. The findings of the present study can be summarized as follows.

- From the experimental study, specimens filled with OCM and NCM show bond failure

between the joint and the precast concrete slabs. In contrast, the PCM embedded specimen exhibits flexural failure, resulting in higher stiffness of the overall structure.

- It is observed that the shapes of the joint are closely related to the mechanical behavior of the road structure, and the maximum principal stress mainly occurs at the area of the slab joints and the power cable hole under a traffic load.
- For the D_2 model, the concentrated stress varies with the depth ratios (a/b) of the slab joints, and the stress near the power cable increases as the depth ratio increases, while the stress at the joint section is inversely proportional to the depth ratios.
- The modulus of the subgrade reaction, indicating the compaction of subgrade soil, significantly affects the overall behavior of the road structures. A high level of soil compaction is expected to improve the stability of the OLEV system.
- A high degree of heat dissipation from the electrical power cable creates considerable thermal deformations, and it is believed to lead reduced strength and stiffness of the OLEV system.
- In case of the road structure with PCM-S, the effects of the friction coefficient between two slabs are negligible. In addition, the stiffness of the surface layer also has an insignificant impact on the OLEV road system. These results indicate that enhancing bonding properties at the contact area and the stiffness of the surface layer may be less important.

The purpose of the experimental and numerical tests conducted herein is to evaluate the efficiency and potential value of modifying the road system in realistic construction environments. The findings from the analyses in this paper may be helpful for those involved in the design of the OLEV system, as they clarify issues related to structural reliability. However, some of these results suggest that there is a need to conduct additional numerical analyses using different designs in an effort to improve the performance and applicability of the recharging road structures.

Acknowledgments

This research was sponsored by the National Research Foundation of Korea (NRF) grants funded by the Korea government (NRF-2012R1A2A4A01008855).

References

- ABAQUS (2010), *6.10 Documentation*, Dassault Systems Simulia Corporation, USA.
- Ahn, S., Chun, Y., Cho, D. and Kim, J. (2011), "Wireless power transfer technology in on-line electric vehicle", *J. Korean Inst. Electromag. Eng. Sci.*, **11**(3), 174-182.
- Ahn, S., Pak, J., Song, T., Lee, H., Byun, J.G., Kang, D., Choi, C.S., Kim, E., Ryu, J., Kim, M., Cha, Y., Chun, Y., Rim, C.T., Yim, J.H., Cho, D.H. and Kim, J. (2010), "Low frequency electromagnetic field reduction techniques for the on-line electric vehicle (OLEV)", *IEEE International Symposium on Electromagnetic Compatibility*, Florida, USA, July.
- Bazant, Z.P. and Oh, B.H. (1983), "Crack band theory for fracture of concrete", *Mater. Struct.*, **16**(3), 155-177.
- Bechtoula, H., Kono, S. and Watanabe, F. (2009), "Seismic performance of high strength reinforced concrete columns", *Struct. Eng. Mech.*, **31**(6), 697-716.
- Boumiz, A., Vernet, F.C. and Tenoudji, F.C. (1995), "Mechanical properties of cement pastes and mortars at early ages: Evolution with time and degree of hydration", *Cem. Mater.*, **3**(3-4), 94-106.
- Chen, E.L., Li, K. and Wang, Y. (2013), "Influence of material characteristics of asphalt pavement to

- thermal stress”, *Appl. Mech. Mater.*, **256-259**, 1769-1775.
- Cho, D. (2012), *Developing the eco-friendly public transportation system based on the wireless power transfer technology*, Land Transport and Maritime, Korea. (in Korean)
- Ellobody, E. and Bailey, C.G. (2011), “Structural performance of a post-tensioned concrete floor during horizontally travelling fires”, *Eng. Struct.*, **33**(6), 1908-1917.
- Fernlund, G., Osooly, A., Poursartip, A., Vaziri, R., Courdji, R., Nelson, K., George, P., Hendrickson, L., Griffith, J. (2003), “Finite element based prediction of process-induced deformation of autoclaved composite structures using 2D process analysis and 3D structural analysis”, *Compos. Struct.*, **62**(2), 223-234.
- George, S.J. and Tian, Y. (2012), “Structural performance of reinforced concrete flat plate buildings subjected to fire”, *Int. J. Concrete. Struct. Mater.*, **6**(2), 111-121.
- Hu, M., Li, L., Wang, Y. and Su, H. (2013), “The application of numerical simulation technology in road engineering”, *Appl. Mech. Mater.*, **336-338**, 690-694.
- Huang, Z.M. (2007), “Failure analysis of laminated structures by FEM based on nonlinear constitutive relationship”, *Compos. Struct.*, **77**(3), 270-279.
- Islam, S.M.S. and Khennane, A. (2013), “Computer aided design of RC structures”, *Int. J. Concrete. Struct. Mater.*, **7**(2), 127-133.
- Jayalekshmi, B.R., Poojary, V.G.D., Venkataramana, K. and Shivashankar, R. (2013), “Seismic response analysis of reinforced concrete frames including soil flexibility”, *Struct. Eng. Mech.*, **48**(1), 1-16.
- Kim, W.J., Lee, J.M., Kim, J.S. and Lee, C.J. (2012), “Measuring high speed crack propagation in concrete fracture test using mechanoluminescent material”, *Smart. Struct. Syst.*, **10**(6), 547-555.
- Lee, H.K., Avila, G. and Montanez, C. (2007), “Numerical study on retrofit and strengthening performance of sprayed fiber reinforced polymer”, *Eng. Struct.*, **27**(10), 1476-1487.
- Lee, I. (2012), *Structural analysis of power supply rail for on-line electric car*, Korea Advanced Instituted of Science and Technology (KAIST), Technical Report. (in Korean)
- Lee, J.M. (2009), “Understanding of DB-load”, *Professional Eng.* **42**, 1-5. (in Korean)
- Liang, Z., Lee, H.K. and Suaris, W. (2006), “Micromechanics-based constitutive modeling for unidirectional laminated composites”, *Int. J. Solids Struct.*, **43**(18-19), 5674-5689.
- Mo, L.T., Huurman, M., Wu, S.P. and Molenaar, A.A.A. (2007), “Investigation into stress states in porous asphalt concrete on the basis of FE-modelling”, *Finite. Elem. Anal. Des.*, **43**(4), 333-343.
- Mo, L.T., Huurman, M., Wu, S.P. and Molenaar, A.A.A. (2013), “Mortar fatigue model for meso-mechanistic mixture design of travelling resistant porous asphalt concrete”, *Mater. Struct.*, DOI: 10.1617/s11527-013-0105-6.
- Ronagh, H.R. and Behnam, B. (2012), “Investigating the effect of prior damage on the post-earthquake fire resistance of reinforced concrete portal frames”, *Int. J. Concrete. Struct. Mater.*, **6**(4), 209-220.
- Sellevoid, E.J. and Bjontegaard, O. (2006), “Coefficient of thermal expansion of cement paste and concrete: mechanisms of moisture interaction”, *Mater. Struct.*, **39**(9), 809-815.
- Shin, E.C., Lee, J.S. and Cho, G.T. (2011), “A study on the frost penetration depth of pavement with field temperature data”, *J. Korean. Soc. Road. Eng.*, **13**(1), 21-32. (in Korean)
- Shin, J., Song, B., Lee, S., Shin, S., Kim, Y., Jung, G. and Jueon, S. (2012), “Contactless power transfer systems for on-line electric vehicle (OLEV)”, *IEEE International Conference on Electric Vehicle*, South Carolina, USA, March.
- Song, S.G., Lee, J.H., Lee, H.J. and Hwang, E.Y. (2005), “Performance evaluation of perpetual asphalt pavements using an accelerated pavements tester”, *J. Korea Soc. Road Eng.*, **7**(3), 1-10.
- Suh, N.P. (2012), “Fundamentals of design and deployment of large complex systems: OLEV, MH, and Mixalloy”, *J. Integ. Des. Proc. Sci.*, **16**(3), 7-28.
- Tahmasebinia, F., Ranzi, G. and Zona, A. (2013), “Probabilistic three-dimensional finite element study on composite beams with steel trapezoidal decking”, *J. Constr. Steel. Res.*, **80**, 394-411.
- Tang, Y., Kusoglu, A., Karlsson, A.M., Santare, M.H., Cleghorn, S. and Johnson, W.B. (2008), “Mechanical properties of a reinforced composite polymer electrolyte membrane and its simulated performance in PEM fuel cells”, *J. Power Sour.*, **175**(2), 817-825.

- Wang, X.S., Chen, T.J. and Ding, X.J. (2011), "Analysis of the mechanical impact of high-modulus asphalt concrete on road structure", *Appl. Mech. Mater.*, **97-98**, 334-339.
- Yang, B.J., Ha, S.K., Pyo, S.H. and Lee, H.K. (2014), "Mechanical characteristics and strengthening effectiveness of random-chopped FRP composites containing air voids", *Compos. Part B: Eng.*, **62**, 159-166.
- Zhou, F. and Young, B. (2012), "Numerical analysis and design of concrete-filled aluminum circular hollow section columns", *Thin. Wall. Struct.*, **50**(1), 45-55.
- Zhu, J., Chen, C. and Han, Q. (2014), "Vehicle-bridge coupling vibration analysis based fatigue reliability prediction of prestressed concrete highway bridges", *Struct. Eng. Mech.*, **49**(2), 203-223.

CC